Draft version May 17, 2022
Typeset using LaTeX **twocolumn** style in AASTeX63

arXiv:2105.04630v2 [astro-ph.HE] 16 May 2022

On the origin of observed cosmic ray spectrum below 100 TV

Mikhail A. Malkov [1] and Igor V. Moskalenko [2]

[1] *Department of Physics and CASS, University of California San Diego, La Jolla, CA 92093, USA*
[2] *Hansen Experimental Physics Laboratory and Kavli Institute for Particle Astrophysics and Cosmology, Stanford University, Stanford, CA 94305, USA*

(Accepted May 15, 2022)

Submitted to ApJ

Abstract

Recent precise measurements of primary and secondary cosmic rays (CRs) in the TV rigidity domain have unveiled a bump in their spectra, located between 0.5–50 TV. We argue that a local shock may generate such a bump by increasing the rigidity of the preexisting CRs below 50 TV by a mere factor of $\sim$1.5. Reaccelerated particles below $\sim$0.5 TV are convected with the interstellar medium (ISM) flow and do not reach the Sun, thus creating the bump. This single universal process is responsible for *the observed spectra of all CR species* in the rigidity range below 100 TV. We propose that one viable shock candidate is the Epsilon Eridani star at 3.2 pc from the Sun, which is well-aligned with the direction of the local magnetic field. Other shocks, such as old supernova shells, may produce a similar effect. We provide a simple formula, Eq. (9), that reproduces the spectra of all CR species with only two nonadjustable shock parameters, uniquely derived from the proton data. We show how our formalism predicts helium and carbon spectra and the B/C ratio.

Keywords: cosmic rays—ISM—reacceleration

1. INTRODUCTION: THE CR "BUMP"

The last decade was marked by discoveries of new features in the spectra of CR species. Unexpected breaks and variations in spectral indices are being unveiled with high confidence in the GV–TV rigidity range that deemed as well-studied (Ahn et al. 2006, 2010; Adriani et al. 2011; Panov et al. 2009; Yoon et al. 2011; Ackermann et al. 2014; Aguilar et al. 2015a,b, 2017, 2018a,b; Aguilar et al. 2020; Atkin et al. 2018, 2019; Grebenyuk et al. 2019a; Adriani et al. 2019; An et al. 2019; Aguilar et al. 2021; Grebenyuk et al. 2019b). These features bear the signatures of CR acceleration processes and their propagation history.

First discovered was a flattening above $R'_{\rm br} \approx 0.5$ TV in rigidity in the CR proton and helium spectra (Ahn et al. 2006, 2010; Adriani et al. 2011), which propelled a slew of interpretations. However, with improved measurements of spectra of several primary (p, He, C, O, Ne, Mg, Si) and secondary[1] (Li, Be, B) species by AMS-02 (Aguilar et al. 2015a,b, 2017, 2018a,b; Aguilar et al. 2020), only two interpretations remain feasible. These are (i) the intrinsic spectral break in the CR injection spectrum or populations of sources with soft and hard spectra, a so-called "injection scenario" (Vladimirov et al. 2012), and (ii) a break in the spectrum of interstellar turbulence translated into the break in the diffusion coefficient, a so-called "propagation scenario" (Vladimirov et al. 2012; Blasi et al. 2012; Aloisio et al. 2015). The latter has very few free parameters and is well-supported (Boschini et al. 2020a,b) by the AMS-02 data.

A turning point was the recent discovery of a steepening in the proton and helium spectra at $R''_{\rm br} \sim 13$ TV (Ahn et al. 2006; Atkin et al. 2018, 2019; Grebenyuk et al. 2019a; Adriani et al. 2019; An et al. 2019), see parameterizations in Boschini et al. (2020b). Together with the lower rigidity break $R'_{\rm br}$, the two features likely result from a single physical process that generates a "bump" in the CR spectrum between

mmalkov@ucsd.edu

imos@stanford.edu

[1] The mostly secondary species are those, which are rare in CR sources, but abundant in CRs. They are produced primarily in fragmentations of heavier species over their lifetime in the Galaxy.

0.5–50 TV. It peaks by a factor of 2.5–3 near ≈13 TV above the background CR spectrum extrapolated from low energies.

The discovery of the second break challenges conventional interpretations of the CR spectra outlined above. This finding also refutes earlier hypotheses of a contribution from a nearby CR accelerator, such as a supernova remnant (SNR), that accelerates the bump particles out of the interstellar medium (ISM) (e.g., Fang et al. 2020; Fornieri et al. 2021; Yuan et al. 2020), because such scenario implies no breaks in the *secondary* component (Vladimirov et al. 2012). Moreover, the unprecedented accuracy with which the sharp break at $R'_{\rm br}$ in the CR spectrum is measured severely constrains its remote or global origins as they would lead to a smoother transition. The recently enhanced data accuracy even allows to identify the dominant turbulent regime through which these CRs propagate from the source to the observer. It was shown to be of Iroshnikov-Kraichnan type (Malkov & Moskalenko 2021, hereafter Paper I).

Another clue to the origin of the bump is the break in the spectra of secondary species that are also flattening above the first break ($R'_{\rm br}$), similarly to the primaries, albeit with a different spectral index. It implies that the secondary species have already been present in the CR mixture that the bump is made of. This leads us to conclude that *(i) the bump has to be made out of the preexisting CRs with all their primaries and secondaries that have spent millions of years in the Galaxy.* Meanwhile, the sharpness of the breaks indicates that *(ii) the bump is formed locally, a short time before we observed it.*

In this paper, we argue that a single universal process is responsible for the observed spectra of all CR species in the rigidity range below 100 TV. We provide a simple formula, Eq. (9), *that reproduces the spectra of all CR species with only two shock parameters derived from a fit to the proton data.* It then fully predicts the entire bump structure including two break rigidities ($R'_{\rm br}$, $R''_{\rm br}$), two respective jumps in the spectral index and two curvatures of the spectrum (sharpness) at the breaks–which would otherwise require six parameters for each CR species. We show how our formalism (Paper I) operates using the proton, helium, and carbon spectra, and the B/C ratio.

2. LOCAL CR REACCELERATION

An immediate consequence of the above-mentioned reasoning is that the bump particles are background CRs reaccelerated inside of the Local Bubble. Estimates show that prospective sources should be within 3–10 pc of the Sun (Paper I). These sources can be of two kinds: point-like and extended. We argue below that the difference between the two is significant. If the source is point-like, it also has an elongated magnetic flux tube. The reaccelerated CRs propagate to the observer through it. Gradual lateral losses from the flux tube and the Iroshnikov-Kraichnan (IK, Iroshnikov 1964; Kraichnan 1965) MHD turbulence driven by the lateral pressure gradient of the reaccelerated CRs critically reshape their rigidity (10-TV bump) and angular spectra that fit to the most accurate recent data. By contrast, propagation of CRs from an extended source through a broad channel without significant lateral pressure gradient and IK-turbulence would require additional assumptions to become consistent with those data.

The bow-shocks and stellar wind termination shocks (TS) of nearby passing stars are obvious candidates of point-like sources. However, most stars can be disqualified as they are not magnetically connected with the heliosphere. Surprisingly, we found a remarkable alignment of the local magnetic field with the Epsilon Eridani star at 3.2 pc from the Sun (Paper I). It also has an extensive 8000 au astrosphere and a thirty times higher than the solar mass loss rate (Wood et al. 2002).

Nevertheless, simple estimates show that even a bow-shock of such a significant size as $\sim 10^4$ au might only marginally reaccelerate preexisting CRs by the required 1.5 factor to generate the bump. On the other hand, this can readily be done by a larger shock. Moreover, as any local shock is likely to be weak, CR species with initially steeper spectra experience a more significant reacceleration (see Eq. [2] in the following section), which is consistent with observations of the secondaries. A particularly appealing source candidate is a sizable imploding shock in the local interstellar medium, whose existence is supported observationally (Gry & Jenkins 2014a), see discussion in Sect. 7.

Notwithstanding the advantage of a large shock, this source is also problematic, as we already mentioned. One serious contradiction comes from the angular distribution of CRs in the bump rigidity range. It rises sharply across the magnetic horizon and also has an enhanced field-aligned component (see Fig. 11 in Abeysekara et al. 2019 and an extended discussion of available data in Paper I). These angular anomalies can be produced simultaneously if a point-like source is located on one side of the flux tube connected to the solar system within several parsecs from the observer. CRs that diffusively propagate from the source along the flux tube also leak through the tube's lateral boundary. Therefore, not all the CRs that passed the observer will return. The observer in the solar system will then see more CRs coming from the source than returning to it. The sharp contrast between these CR groups on the intensity map is critically associated with the IK spectrum of the scattering turbulence. The field-aligned component is not related to the CR losses but follows the solution of the complete Fokker-Plank transport problem, not limited by the diffusive approximation. It was shown (Malkov 2017) that the field-aligned component survives a longer propagation from the source (up to 5-7 particle mean free paths) than might have been expected.

Despite the rise at the CR pitch-angle of 90° (magnetic horizon) and the field-aligned one-sided enhancement have different physical causes, their coexistence have been demonstrated (Paper I) by solving the proper CR propagation with lateral losses and the IK pitch-angle scattering. To our best knowledge, no other CR source and transport regime configuration fits the current data in 1-100 TV range with dramatically shrunk statistical uncertainties (Aguilar et al. 2021, see also Fig. 1 below).

The current data are so accurate and multifaceted (rigidity-, angular-, and chemical composition spectra) that the "reverse engineering" of the 10-TV bump source and its propagation mode became possible without identifying any particular object presumably responsible for the bump. Still, the source is likely associated with a shock, whose parameters can be constrained, but the shock may remain invisible in the sky. In the Appendix, we provide a brief discussion of potentially qualified shocks.

The situation with a well-described but unknown source is not entirely satisfactory, so we pursue two parallel approaches to improve it. One approach is to develop a "generic" shock reacceleration and CR propagation model along a magnetic flux tube pointing to the solar system. It depends on an unknown shock Mach number and its size-distance relation (Paper I). The model's key advantage is that these parameters are uniquely derived from the best measured CR proton spectrum or its substitute. As the latter, we use "synthetic" data provided in Boschini et al. (2020b), i.e., a physically motivated local interstellar spectrum (LIS) of CR protons tuned to the data of different instruments with adjustments for the appropriate heliospheric modulation. As the slope and normalization of CR background LIS below the first break are now accurately derived (Boschini et al. 2020b), the model takes them as fixed input parameters. The turbulence index, found to be $s = 3/2$ (IK spectrum), critically determines the proton spectrum, yielding the precise spectral shape over four orders of magnitude in rigidity (Paper I). To further test our model, we turn to other species.

The second approach is to look at the Epsilon Eridani star as it is magnetically connected with our Sun and its distance is also in the right ballpark. However, as we noted, its bow shock is somewhat weak, making the reacceleration of CR of several tenths of TV problematic. This issue can be ameliorated considering that the bow shock and strong stellar wind TS coexist in the system, while the resulting bump spectrum is still primarily shaped during the CR propagation. We provide the corresponding formalism in the Appendix. In the following section, we review and extend to a broader geometrical setting a generic CR reacceleration and propagation model developed in Paper I. We now include the lateral particle losses in this model.

3. CR REACCELERATION AND PROPAGATION MODEL

Only two parameters, constituting the bump amplitude, K, and rigidity, R_0, suffice to predict the bump spectrum (Paper I) without particle losses from the flux tube. The reaccelerated CR density is elevated over the background by the factor

$$K = (\gamma+2)/(q-\gamma), \tag{1}$$

where γ is the spectral index of the background CRs and $q > \gamma$ is that of the shock, $q = (r+2)/(r-1)$. Here r is the shock compression ratio, which we determine from the proton fit. The enhanced spectrum appears as a bump at some distance from the shock, as the reaccelerated CR with lower rigidity do not reach the observer. There will also be a high-energy cutoff to the CR enhancement, associated with the particle losses from the flux tube and the limited shock size, which we also discuss later.

The background CR spectrum is $f_\infty \propto R^{-\gamma}$, whereas the shock would accelerate the freshly injected thermal particles to R^{-q} spectrum. However, as the shock is likely to be weak, that is $q > \gamma \approx 2.85$ (for protons), the freshly accelerated CRs are submerged into the reaccelerated CR component. The CR density measured at a distance z from the shock is (Blandford & Ostriker 1978, Paper I):

$$f(R,z) = f_\infty(R)\left[1 + Ke^{-\Phi(R,z)}\right], \tag{2}$$

where K is defined in Eq. (1). The flux suppression exponent, Φ, is a path integral of particles propagating along the magnetic flux tube from the shock. One may distinguish between two cases of the relative motion of the shock and the observer, although the rigidity dependence of $\Phi(R)$ is similar in both cases.

3.1. *Propagation from quasi-parallel portions of shock*

If the shock normal makes an angle ϑ_{Bn} with respect to the local magnetic field not too close to $\pi/2$, the CR distribution along the flux tube is determined by the balance between the CR convection with the flow and diffusion against it. In this case we have

$$\Phi = u\int_0^z \frac{dz}{\kappa_\parallel(R,z)} + \mathscr{L}(R). \tag{3}$$

Here $u = u_{sh}/\cos\vartheta_{Bn}$ with u_{sh} being the shock velocity, and $\kappa_\parallel$ is the parallel component of the diffusion tensor. The term $\mathscr{L}(R)$ describes lateral losses from the flux tube. The bump characteristic rigidity R_0 is introduced by the relation $\Phi \approx (R_0/R)^{1/2} + \mathscr{L}$. Here the power $1/2$ corresponds to the IK turbulence. The parameter R_0 combines the distance to the shock, z, velocity u and the turbulence power, that defines $\kappa_\parallel$ in Eq. (3). According to Paper I, $R_0 \propto u^2 z^2/l_\perp$ where the characteristic scale of the CR pressure gradient across the

flux tube is $l_\perp^{-1} = P_{\rm CR}^{-1}\partial P_{\rm CR}/\partial r$. It sets the amplitude of magnetic perturbations driven by this gradient.

3.2. *Propagation from quasi-perpendicular portions of shock*

In the case $\vartheta_{Bn} \approx \pi/2$, satisfied at some fraction of almost any curved shock, we use the balance between the divergence of convective and diffusive CR fluxes in the shock frame, $v\cdot\nabla F \sim \nabla_\parallel \kappa_\parallel \nabla_\parallel F$, which is consistent with Eqs. (2)–(3). Here F is the full-bump distribution related to f below. The CR diffusion proceeds primarily along the field, but the convective term is $v\cdot\nabla F \approx v_\perp\cdot\nabla_\perp F$, which we may write assuming the ISM wind being in y-direction and magnetic field in z-direction. So we have $v\partial F/\partial y \approx \kappa_\parallel \partial^2 F/\partial z^2$, assuming that $\kappa_\parallel$ is independent of z, for a simple illustration. The result will then have a similar to the former case exponential dependence,

$$\propto \exp\left[-vz^2/4y\kappa_\parallel(R)\right]. \tag{4}$$

Averaging over y, or rather over radial coordinate inside the tube, $r_\perp$, depends on the shock structure and CR propagation in the tube that controls the losses.

3.3. *Lateral Losses of CRs*

Lateral losses from the flux tube affect high-rigidity end of the 10-TV bump, roughly between 10-50 TV. Our goal is to include them in a way applicable to different CR propagation regimes. Assuming a quasi-stationary distribution of reaccelerated CRs around a moving reaccelerator (e.g., a stellar bow-shock) we balance the following channels of particle transport: convection along the field, two components of diffusion (parallel and perpendicular to the B-field), and the lateral losses.

If the convective transport is significant, it is convenient to use the bump component $f_{\rm b}(R,z) \equiv f - f_\infty$ in Eq. (2) as a radially averaged part of its full distribution, F. Namely, $f_{\rm b} = 2a_\perp^{-2}\int_0^{a_\perp} F(R,z,r_\perp)\, r_\perp dr_\perp$, where $a_\perp$ is the tube's radius. The CR flux at $r_\perp = a_\perp$ is $-2\pi\kappa_\perp \partial F/\partial r_\perp|_{r_\perp=a_\perp}$. Here $\kappa_\perp$ is a cross-field component of the CR diffusion tensor. Particle losses from the flux tube depend on the distance from the source because the self-driven turbulence decreases with it. We use the following general relation between the two components of κ, (e.g., Drury 1983), $\kappa_\perp \approx \kappa_B^2/\kappa_\parallel \approx \kappa_B k\delta B_k^2/B^2$, where $\kappa_B = cr_g/3$ is the Bohm diffusion, r_g is the Larmor radius, and $\delta B_k^2 \ll B^2/k$ is the spectral energy density of Alfven waves evaluated at the resonant wave number $k = r_g^{-1}$. Alfvenic fluctuations inside the magnetic flux tube filled with reaccelerated CRs were shown to obey the Iroshnikov-Kraichnan law, $\delta B_k^2 \propto k^{-3/2}$ (Paper I). In this case, $\kappa_\perp \propto R^{3/2}$, while $\kappa_\parallel \propto R^{1/2}$. It follows that for large R the path integral Φ in Eq. (3) will be dominated by the second term, associated with lateral particle losses from the tube rather than their propagation along the field (the first term).

If the CR source velocity has a sizable component along the B-field the lateral losses are balanced by the CR convection along the field. The diffusion in that direction is suppressed because of the self-driven IK-turbulence. The CR flux from the magnetic tube, $-2\pi\kappa_\perp\partial F/\partial r_\perp|_{r_\perp=a_\perp}$, can be estimated by recognizing that the fluctuation level must drop at the tube's edge, $r_\perp = a_\perp$, as these fluctuations are driven by the excessive pressure of reaccelerated CRs inside the tube. Beyond this radius, CRs diffuse primarily along the field, since the level of the background ISM fluctuations is typically very small, $k\delta B_k^2/B^2 \sim 10^{-5}$ at a scale $\sim 10^{12}-10^{13}$cm (e.g., Achterberg et al. 1994). Hence, the scattering events resulting in the displacement of the particle guiding center are increasingly rare.

Upon reaching the edge of the flux tube particles almost instantaneously escape along the field, since $\kappa_\perp \sim k^2(\delta B_k/B)^4\kappa_\parallel \ll \kappa_\parallel$, notwithstanding the tube's length being much larger than its lateral size. Under these conditions, the most plausible estimate for $\partial F/\partial r_\perp|_{r_\perp=a_\perp}$ is $\sim -F/r_g$. The CR flux through the lateral boundary of the tube scales with rigidity as $\sim\kappa_\perp F/r_g \propto R^{1/2}F$. An equilibration of convective CR transport $v\cdot\nabla F$ with these losses yields the following approximate relation $v_z\partial f_b/\partial z \approx -\kappa_\perp f_b/r_g a_\perp$. Here v_z is the projection of the CR source velocity on the field direction. We thus obtain the following exponential decay of the CR density along the tube: $f_b \propto \exp\left[-\sqrt{R/R_L}\right]$. Here $R_L \propto 1/z^2$ is the rigidity cut-off associated with the lateral losses and z is the current distance to the source. The cut-off R_L also depends on the flow geometry and details of the CR escape that we discussed using only order of magnitude estimates above. Therefore, the path integral in Eq. (3) at fixed z can be represented as

$$\Phi = (R_0/R)^{1/2} + (R/R_L)^{1/2}. \tag{5}$$

Fortunately, the same form of high-rigidity cut-off is applicable when the convective transport is negligible because of the flow geometry, i.e., $v_z \approx 0$. In this case the lateral CR diffusion is balanced by that along the field:

$$\frac{\partial}{\partial z}\kappa_\parallel\frac{\partial F}{\partial z} + \frac{1}{r_\perp}\frac{\partial}{\partial r_\perp} r_\perp\kappa_\perp\frac{\partial F}{\partial r_\perp} = 0. \tag{6}$$

After substituting $\kappa_\perp = \kappa_B^2/\kappa_\parallel$, assuming that $\kappa_\parallel$ is separable, i.e., $\kappa_\parallel = \kappa_0(R)\,\kappa_1(r_\perp)\,P(z)$, and introducing a new variable $\zeta = \int_0^z dz/P$, the last equation rewrites as follows

$$\frac{\kappa_0^2}{\kappa_B^2}\frac{\partial^2 F}{\partial\zeta^2} + \frac{1}{r_\perp\kappa_1}\frac{\partial}{\partial r_\perp}\frac{r_\perp}{\kappa_1}\frac{\partial F}{\partial r_\perp} = 0. \tag{7}$$

This equation can be solved by separating the variables $F = \Psi(\zeta)\,\phi(r_\perp)$:

$$\frac{\kappa_0^2}{\kappa_B^2}\frac{1}{\Psi}\frac{\partial^2\Psi}{\partial\zeta^2} = -\frac{1}{r_\perp\kappa_1\phi}\frac{\partial}{\partial r_\perp}\frac{r_\perp}{\kappa_1}\frac{\partial\phi}{\partial r_\perp} = \lambda^2,$$

where λ^2 is a separation constant, which is also the spectral parameter of the problem for ϕ defined by the boundary conditions $\phi(r_\perp = a_\perp) = 0$ and the requirement of regularity of ϕ at $r_\perp = 0$ imposed on the second equation above. For $\kappa_1 = const$, its solution is given by Bessel function, J_0, $\phi_n(r_\perp) = J_0(\mu_n r_\perp/a_\perp)$, where μ_n is its n-th root, $J_0(\mu_n) = 0$, $\mu_1 \approx 2.5$, $\mu_2 \approx 5.5, \ldots$ In this case, the spectrum is $\lambda_n = \mu_n/a_\perp\kappa_1$. For $\kappa_1(r_\perp) \neq const$, the eigenvalues $\{\lambda_n\}_{n=1}^{\infty}$ also grow rapidly with n. Therefore, expanding the solution of Eq. (7) in a series of eigenfunctions $\{\phi_n\}_{n=1}^{\infty}$ with coefficients $\Psi_n(\zeta, R)$,

$$\Psi_n = C_n(R)\exp\left\{-\lambda_n\frac{\kappa_B}{\kappa_0}\int_0^z dz/P\right\},$$

we can retain only the first term in the series at the observer position z. Note, that particle rigidity, R, enters Eq. (6) as a parameter, so that the solution can be represented as follows

$$F = \sum_{n=1}^{\infty}\Psi_n(\zeta, R)\,\phi_n(r_\perp) \approx C_1\phi_1\exp\left\{-\lambda_1\frac{\kappa_B}{\kappa_0}\int_0^z\frac{dz}{P}\right\}. \quad (8)$$

The prefactor $C_1(R)\,\phi_1(r_\perp)$ is determined by the spectrum generated by the reaccelerator and the near-zone propagation. Considering the CR reacceleration at a generic shock wave, for example, C_1 includes the background CR spectrum (f_∞ in Eq. [2]) and the first term in Eq. (3) or Eq. (4). The choice between the two depends on the accelerator's motion relative to the observer and the ambient B-field, as considered earlier in this section. In either case, the exponential dependence on rigidity is in the form given by the first term in Eq. (5). Nevertheless, different expressions for the CR bump parameter R_0 apply, as considered in Paper I in more detail. The significance of the result in Eq. (8) is that the exponential rigidity cut-off has the same form as in Eq. (5), $\exp\left(-\sqrt{R/R_L}\right)$. This follows from the relation $\kappa_B/\kappa_0 \propto \sqrt{R}$ that we have discussed earlier.

To conclude this section, the CR bump-defining factor, $\exp[-\Phi(R)]$, is generically given by Eq. (5) with two parameters R_0 and R_L that can be determined analytically (see above and Paper I for detailed calculations), depending on the particular reacceleration scenario. Alternatively, they can be extracted from fitting this formula to the data (next section). As this factor bears more on propagation and losses than reacceleration, it can also be applied to the case of CR reacceleration at a stellar TS, which we consider in detail in the Appendix. It boosts the stellar bow-shock reacceleration, thus easing the observational constraints on the observed CR bump.

4. PROBING THE SHOCK WITH REACCELERATED PROTONS

Following the formalism developed in Paper I and the results of the preceding section, we represent the spectrum of an arbitrary CR species in the following form, Eqs. (2), (5):

$$f_s(R) = A_s R^{-\gamma_s}\left\{1 + \frac{\gamma_s + 2}{q - \gamma_s}\exp\left[-\sqrt{\frac{R_0}{R}} - \sqrt{\frac{R}{R_L}}\right]\right\}, \quad (9)$$

where A_s and γ_s are the normalization and spectral index of CR species ($s = p$, He, B, C, ...) that will be fixed using the data at $R \ll R_0$ (the so-called background CRs). These data are not related to the bump phenomenon described by the remaining three parameters: q, R_0, and R_L, where, $q = (r+2)/(r-1) > \gamma_s$.

In the first step we remotely sense the shock parameters using the precision measurements of the local proton spectrum. The best available data in the GV–TV domain are provided by AMS-02, CALET, and DAMPE (Aguilar et al. 2021; Adriani et al. 2019; An et al. 2019). To mitigate the systematic discrepancies between these instruments we use overlaps of their rigidity ranges as follows.

The most accurate measurements are provided by AMS-02, which has several independent systems that allow for data cross checks. To eliminate the solar modulation effects below the first break rigidity, we use the proton LIS (Boschini et al. 2020b), which was derived using the AMS-02 data. The CALET and DAMPE data are then modified to normalize their first break rigidity $R'_{\rm br}$ and their flux at $R'_{\rm br}$ (minimum in the spectrum in Fig. 1) to the values derived from the proton LIS. This was achieved by applying the following transformations: $R = \tilde{R}/1.12$, Flux$= \widetilde{\rm Flux}\times 1.09$ to CALET, and $R = \tilde{R}/0.95$, Flux$= \widetilde{\rm Flux}\times 0.98$ to DAMPE data. Here $\tilde{R}$ and $\widetilde{\rm Flux}$ are the published rigidity and flux values (Adriani et al. 2019; An et al. 2019). These adjustments are well within the instrumental error bars. The model parameters derived from the best fit to the modified data of all three instruments are summarized in Table 1.

The LIS spectra below the break were used to obtain the model input parameters listed in Table 2. Fig. 1 shows the proton data along with two models, where we have considered the cases of loss-free (LF) model $R_L = \infty$ and realistic model (RM) $R_L < \infty$, which is more accurate for $R \gtrsim R''_{\rm br}$. The RM model provides a better match of the data above 10 TV indicating that the shock size or other geometry constraints are at play. *Regardless of their nature, all model parameters, q, R_0, R_L, are now fixed.*

5. CALCULATING SPECTRA OF OTHER ELEMENTS

According to Eq. (9), the species are differentiated solely by their spectral index γ_s below the break $R'_{\rm br}$. We illustrate this in Fig. 2, where we use the spectral indices corresponding to the helium and boron LIS, and an arbitrary index corresponding to a steeper spectrum, $\gamma_{\rm arb} = 3.7$. One can see

Table 1. Model parameters and fit results for the proton spectrum.

Parameter (St. err. %)	R_0(GV)	R_L(GV)	q	$K=(\gamma+2)/(q-\gamma)$	$\chi^2_{\rm min}$/dof	dof
Realistic Model (RM)	5878 (3.5%)	2.24×10^5 (28%)	4.2	3.59 (4.9%)	0.10	76-3
Loss-Free Model (LF)	4795 (3.2%)	∞	4.7	2.58 (2.9%)	0.19	76-2

Table 2. Input parameters for CR species derived from their LIS (Boschini et al. 2020b).

Parameters	protons	helium	boron	carbon
A_s (m^{-2} s^{-1} sr^{-1} GV^{-1})	2.32×10^4	3410	79	109
γ_s	2.85	2.76	3.1	2.76

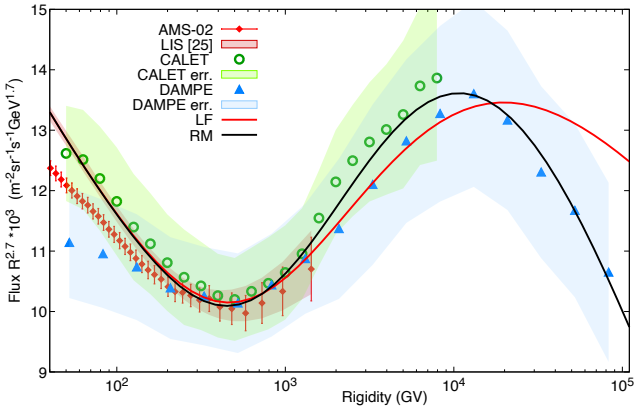


Figure 1. Proton rigidity spectrum from AMS-02, CALET, and DAMPE (Aguilar et al. 2021; Adriani et al. 2019; An et al. 2019). CALET and DAMPE data were modified to adjust for systematic differences between the three instruments, see text for details. The curves show the model calculations, Eq. (9), for the cases of $R_L=\infty$ (LF model) and a more realistic for high rigidities case of finite losses $R_L<\infty$ (RM model). The model and input parameters are summarized in Tables 1, 2.

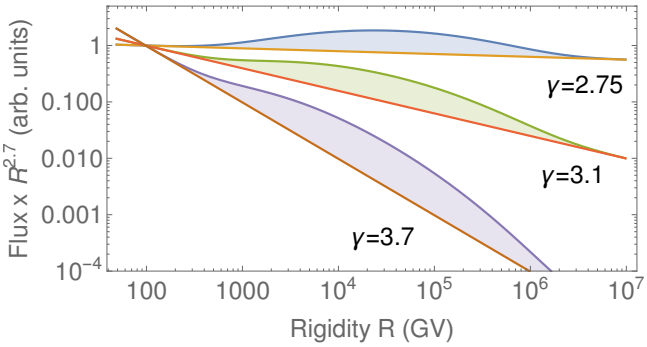


Figure 2. The bump strengths in the CR spectra with different spectral indices corresponding to the helium and boron LIS (Table 2), and $\gamma_{\rm arb}=3.7$ (for illustration), calculated using Eq. (9) and compared to the straight background power-laws. The ratios of the enhanced fluxes at $R=30$ TV to the background values for the three different values of γ are 2.46, 3.06, and 6.05, respectively.

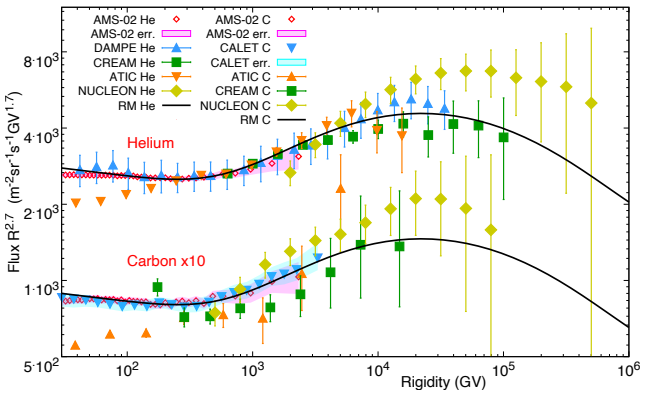


Figure 3. The calculated helium and carbon spectra are compared with available helium data from AMS-02, DAMPE, CREAM, ATIC, and NUCLEON (Aguilar et al. 2021; Alemanno et al. 2021; Karmanov et al. 2020b; Panov et al. 2009; Yoon et al. 2017) and carbon data from AMS-02, CALET (multiplied by 1.27), ATIC, CREAM, and NUCLEON (Ahn et al. 2009; Adriani et al. 2020; Aguilar et al. 2021; Karmanov et al. 2020a). The RM model calculations are using Eq. (9) with parameters provided in Tables 1, 2.

that CRs with steeper background spectra undergo stronger reacceleration.

Fig. 3 shows the primary helium and carbon spectra. The DAMPE and CREAM helium spectra were normalized to the helium LIS by applying factors 1.08 and 1.05, correspondingly. Following Adriani et al. (2020) the CALET spectrum of carbon was multiplied by 1.27 to agree with AMS-02 data. Given the same spectral indices below the first break $R'_{\rm br}$, the shapes of helium and carbon spectra are identical.

We are also comparing our model calculations with the measurements of the B/C ratio that is widely used to evaluate the CR residence time in the Galaxy. It is measured in a wider rigidity range and with higher precision than the individual spectra of boron and carbon. Fig. 4 shows the calculated B/C ratio compared with available data. The inset shows the ratio multiplied by a factor $R^{0.3}$ to emphasize the fine details in the bump range. Our model shows ≈10% deviation from predictions for the Kolmogorov turbulence $\propto R^{-0.33}$ (Kolmogorov 1941) in the bump range.

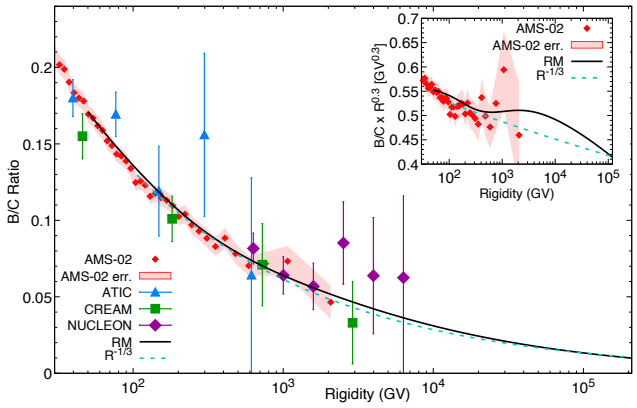


Figure 4. The calculated B/C ratio is compared with AMS-02, CREAM, ATIC, and NUCLEON data (Aguilar et al. 2021; Ahn et al. 2008; Grebenyuk et al. 2019b; Panov et al. 2008). The RM model calculations are using Eq. (9) with parameters provided in Tables 1, 2.

6. BACKGROUND SPECTRA

Here we comment on the origin of the background spectra of different CR species below $R'_{\rm br}$. A physical explanation for the observed difference between γ_p and γ_s of primary elements with effective mass to ion-charge ratios $\langle A/Q\rangle \approx 2$, or higher has already been suggested (Malkov 1998; Malkov et al. 2012; Hanusch et al. 2019). They develop harder than proton spectra (the index difference $\gamma_p - \gamma_s \approx 0.1$) because SNR shocks extract them from thermal plasma most efficiently when these shocks are at their strongest. The time-integrated spectra of heavier elements become then harder than that of the protons.

This bias stems from the shock related turbulence whose amplitude increases with the Mach number. Resonantly driven by protons, it curbs them tighter downstream than heavier nuclei, so the latter may cross the shock to gain energy. As the above differentiation mechanism depends exclusively on $\langle A/Q\rangle$, its salient consequence is that all elements with the same $\langle A/Q\rangle$ must have the same ultrarelativistic rigidity spectra (Malkov 2018). No exceptions to this rule have been reported so far (Aguilar et al. 2021).

The steep background spectrum of the secondaries is related to a decreasing residence time of CR species in the Galaxy as rigidity increases. The secondaries are already produced in fragmentations of primary CRs with a steep spectrum that is further steepened due to the rigidity-dependent residence time.

7. DISCUSSION

There is no reason to believe that the observed bump in the CR spectrum is unique. Similar bumps might be generated in other Galactic locations where shocks are present. Whether their integral contribution competes favorably with the CR reacceleration by the ISM turbulence is too early to say. Theoretical estimates of the turbulent reacceleration (Seo & Ptuskin 1994; Ptuskin et al. 2006; Drury & Strong 2017) suggest that it supplies up to 50% of the power required to maintain the CRs against losses. However, this estimate is difficult to confirm using observations, as the reaccelerated CRs are inseparable from the background.

By contrast, a contribution of CR-reaccelerating shock is identifiable and, as we argued, is currently observed. The next step is to create an inventory of such shocks and integrate their contributions. Our results show that such shocks can temporarily modify the local CR spectrum. Studies of time-dependent CR transport show similar modifications (Porter et al. 2019). However, the significance of our result is that we do not need such a major event as a supernova explosion nearby to modify the local CR spectrum.

The local interpretation of the 10-TV bump has broader consequences in terms of our understanding of the CR spectrum. First, the B/C ratio is also affected by such modifications. Hence, the observed B/C ratio cannot be used to estimate the CR confinement time without corrections for the reacceleration effects due to the passing stars and other shocks in the local interstellar medium. We speculate that even the well-known "knee" at ∼3 PV could also be interpreted as a "big bump" in the following fashion. The spectrum hardens below the knee due to a reacceleration by some shock, which is consistent with observations. How exactly it hardens is not clear since these observations are not nearly as accurate as the new observations in the region $\lesssim 10$ TV discussed in this paper. The "local" shock that might be responsible for the reacceleration needs to be 2-3 orders of magnitude larger, e.g., a spiral density shock (Shu et al. 1972). According to Eq. (2), weaker shocks substantially affect steep background CR spectra. The knee itself is then generated by physical processes similar to those responsible for the 10-TV bump formation addressed earlier.

Returning to the subject of this paper, let us discuss possible local CR reaccelerators. Apparently, the reacceleration power requirements are modest because the background CR spectrum is steep ($\propto R^{-2.85}$). Its slight upshift (by a factor ≈ 1.36) in rigidity suffices for the bump to be formed. However, its fine structure depends on the self-generated turbulence (Paper I), through which the reaccelerated CRs propagate to the observer along the magnetic field. The low-energy reaccelerated particles ($R \lesssim 1$ TV) do not reach the observer as they are convected downstream with the ISM flow. This low-energy screening makes the distance to the object a defining parameter for the bump.

A more detailed formalism in Paper I shows that the observed bump is a factor 2.4 enhancement over the background spectrum at its maximum near 10 TV (after the spectrum is multiplied by $R^{2.7}$). Even a weak shock of a size comparable with the particle Larmor orbit can provide the required up-

shift, operating in an SDA regime (shock-drift acceleration). All it takes is that the shock overruns a significant portion of the particle Larmor orbit before the particle escapes the shock front along the field line. The full orbit crossing-time is $r_g/U_{\rm shock} \approx$30 yrs for $r_g \sim 3\times10^{15}$ cm (a 10-TV proton in a 10 μG field [2]) and $U_{\rm shock} \approx 30$ km sec^{-1}. The flow near the shock front is likely turbulent, so the particle confinement in the field direction can be taken at the Bohm level. Particles do not diffuse beyond $\sim r_g\sqrt{c/U_{\rm shock}}$ from the shock during the orbit crossing.

While these numbers appear restrictive for the Epsilon Eridani bow shock, which is 8000 au $\sim 10^{17}$ cm, it can still cross orbits of 10-TV particles before they diffuse away along the field. The bow shock tail may even exceed 10^4 au. Because the quasi-one-dimensional diffusion of particles along the field is recurrent, they will have a fair chance to interact with the shock repeatedly and climb up its flanks to the apex, thus gaining more energy via the SDA process. Stronger nondiffusive confinement of particles to a bow shock near its head is also possible by modifying the shock magnetic environment by energetic particles themselves. For example, such phenomena are observed at the Earth's bow shock (magnetic cavities, hot flow anomalies, etc., Sibeck et al. 2021). In addition, the diamagnetically expelled field ahead of the shock may create a magnetic trap for the particles, thus extending their interaction with the shock (see Appendix). The particle energy gain after a single Larmor-circle shock crossing can be inferred from the conservation of the particle magnetic moment: $p_\perp^2/B = const$, where $p_\perp$ is the perpendicular to the B-field component of particle momentum. Therefore, even a factor of two magnetic field compression would suffice to make the bump visible.

The above constraints on the energy gain may be further relaxed in the case of a powerful stellar wind TS (e.g., Epsilon Eridani star), as the shock speed is likely to exceed the bow-shock velocity by two orders of magnitude (see Appendix). In addition, the Cranfield-Axford effect (Axford 1972) may substantially increase the magnetic field in the surrounding area filled by the shocked stellar wind. Analytic models for the CR spectrum re-power by the stellar terminal shocks are available (e.g., Webb et al. 1985), showing a relatively high, typically 40% efficiency of the wind energy conversion into the reaccelerated CRs. Observations also indicate that powerful stellar winds accelerate particles efficiently (Rangelov et al. 2019).

Shocks that are significantly larger than stellar bow-shocks are almost certainly present in the solar system proximity and can remove the maximum energy restrictions. We have discussed possible origins and even tantalizing evidence for their existence in the Local Bubble (Gry & Jenkins 2014b; Paper I). However, the Epsilon Eridani is particularly appealing being well-aligned with the direction of the local magnetic field, yet fitting the basic model restrictions. A serious contradiction of a large-shock scenario comes from the angular distribution of the bump particles. It is much easier to reconcile the anisotropy data with a smaller shock and a narrow propagation channel pertinent to the Epsilon Eridani. We, therefore, provide in the Appendix a compound acceleration model tailored for this star in which both the bow-shock and the stellar wind TS are synergistically involved in the SDA process.

ACKNOWLEDGMENTS

We thank Samuel Ting, Andrei Kounine and Vitaly Choutko for numerous discussions of the AMS-02 data, John Krizmanic, Kazuyoshi Kobayashi, and Shoji Torii for discussions of the CALET data, Jin Chang and Qiang Yuan for providing the DAMPE data prior to their publication and discussions, Dmitry Podorozhny, Alexander Panov, and Andrey Turundaevsky for providing the updated data of NUCLEON and ATIC, and Eun-Suk Seo for providing the CREAM data. We also acknowledge numerous discussions with Pat Diamond. Mikhail A. Malkov acknowledges support from NASA ATP-program within grant 80NSSC17K0255 and from the National Science Foundation under grants No. NSF PHY-1748958 and AST-2109103. Igor V. Moskalenko acknowledges support from NASA Grants No. NNX17AB48G, 80NSSC22K0718, 80NSSC22K0477.

APPENDIX

A. COMPOUND ACCELERATION MODEL

The purpose of this Appendix is to demonstrate that under a favorable but realistic B-field configuration, the interaction of particles with the TS is longer than in the standard SDA (shock-drift acceleration) cycle and results in a larger than the $\Delta p_\perp/p_\perp \approx \sqrt{r}$ momentum gain, where r is the compression ratio. We show that the interaction of star's bow shock with its wind TS in the Epsilon Eridani system and its peculiar location makes it a viable candidate source of the observed 10-TV CR bump.

[2] The direct measurements of Voyager 1, 2 give 7-8 μG just outside of the heliosphere (Burlaga et al. 2019).

A.1. *Motivation and Physical Context*

A particle acceleration model that would combine a star's bow shock with its wind TS is motivated by overwhelming evidence of the Local Bubble origin of 10-TV bump, discussed in the Introduction. The potential efficiency of this model is supported by studies of colliding plasma flows in astrophysical (e.g., Bykov 2001) and laboratory (e.g., Malkov & Sotnikov 2022) settings. Here we focus on a collision region between the stellar wind and the inflowing ISM wind.

The absence of traditional CR sources, such as SNRs, in our proximity raises the bar for potential accelerator efficiency. In Paper I, we entertained the following three types of possible sources: (i) a radiative shell of an old SNR or magnetoacoustic shock formed by wave steepening, (ii) imploding shock within a monolithic Local Bubble model inferred by Gry & Jenkins (2014b) from their observation analysis, and (iii) a stellar bow-shock. Shocks from (i) and (ii) variety, being comparable in size with the distance to them, easily provide the required flux of reaccelerated CRs into the 10-TV range at the observer's location. Indeed, lateral losses of CRs from the flux tube in Eq. (9) are not important, given a significant size-to-distance ratio of such source. By contrast, this ratio is rather small even for a nearby stellar bow-shock and the lateral spread of reaccelerated CRs might make the bump unobservable near the Sun. On a potentially positive side, the bow-shock scenario provides a unique opportunity to associate the observed CRs with familiar objects, thus increasing the persuasiveness of this scenario. Adding the serendipitously close (within 6.7°) alignment of a nearby (ca. 3.2 pc) Epsilon Eridani star with the local magnetic field direction warrants a closer look at this object as a likely source of the CR bump.

Our interest in this object is also driven by the angular distribution of CRs in the rigidity range where the observed CR bump is located. We have discussed this aspect of the bump phenomenon in Paper I (see Sect. 7 and Appendix D). We have shown that if the source of the bump is located on one side of the magnetic field line in a limited range of 3-10 pc, the observed spectrum will have an anisotropy characterized by a sharp raise across the magnetic horizon, which is actually observed. Sources, located at larger distances would have produced a much smoother angular CR distribution. This is equally true for the rigidity dependence of the CR spectrum in the bump area, discussed earlier.

Estimates of the energy gained by particles after crossing a stellar bow shock (Sect. 7) and the propagation losses (Sect. 3) demonstrate that the Epsilon Eridani's bow-shock can marginally account for the bump in terms of its magnitude. At the same time, additional losses, e.g., those discussed in Paper I may raise the required CR reacceleration rate at the source. We therefore consider a possibility of CR reacceleration at the *stellar wind TS as a booster* for particles that have already passed through the bow-shock and increased their energy, Fig. 5.

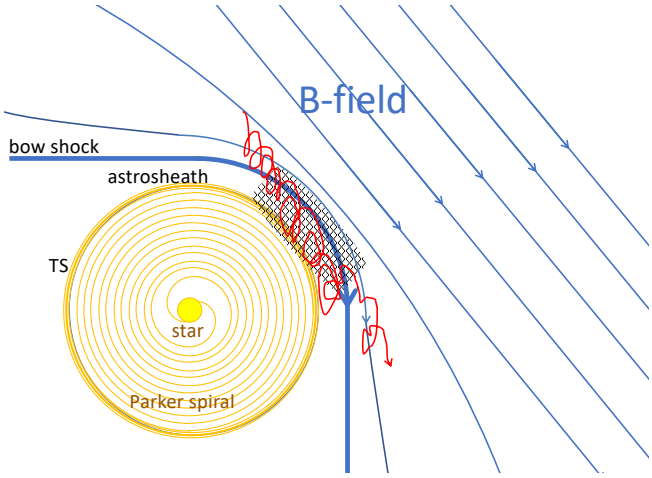


Figure 5. Stellar wind cavity showing the TS and bow-shock ahead of a moving star. The hatched area covering the adjacent portions of bow-shock and TS is a magnetic trap for CRs (see text).

A.2. *Model Description and Estimates of its Efficiency*

Let us first consider plasma conditions in the region between the stellar wind TS and the bow-shock that includes the astropause (that can be characterized as such using its analogy with the heliopause). This is a turbulent zone of colliding flows where thermal particles may undergo stochastic acceleration (e.g., Brunetti & Lazarian 2007; Lemoine 2021). However, their energy would not be sufficient to reach the solar system, so we focus on the reacceleration of preexisting CRs.

Particles with energies up to tenths of TeV have Larmor radii comparable with the thickness of the shocked plasma layer between the bow-shock and TS. Gyrating along this layer, as shown in Fig. 5, they visit the stellar wind cavity where a motion electric field $E \sim U_{\rm SW}B/c$, accelerates them. Here $U_{\rm SW}$ is the velocity of the stellar wind. As their perpendicular momentum increases by a factor $\Delta p_\perp/p_\perp \sim U_{\rm SW}/c$ each time they cross and recross the TS, the pressure of CRs in this area (shown by a hatched rectangle in Fig. 5) is higher than the ambient CR pressure. By the pressure balance, the field strength should be lower in this area, thus developing a magnetic cavity. We may ignore the effect of the ISM wind ram pressure of the inflowing plasma for now, as the star velocity is relatively low, ≈ 30 km s^{-1}. However, cumulative effects of the magnetic flux expelled from the cavity, flow compression behind the shocks, involvement of neutrals, and general flow pattern past the astrosphere result in a magnetic barrier around the cavity. Therefore, not only the particles inflowing from the bow-shock apex with $p_\perp \gg p_\parallel$ become trapped, but also field aligned particles around the cavity have a good chance to be trapped adiabatically into the magnetic

cavity and stay there, as they are scattered in pitch angle. The adiabatic trapping into magnetic cavity is quite similar to that into an electrostatic potential well, as described by Gurevich (1968). We, therefore, omit the details and focus on the interaction of the trapped particles with the TS.

A.3. *Dynamics of Trapped Particles*

The purpose of this analysis is to demonstrate that under a favorable but realistic B-field configuration, the interaction of particles with the TS is longer than in the standard SDA (shock-drift acceleration) cycle and, therefore, results in a larger than the $\Delta p_\perp/p_\perp \approx \sqrt{r}$ momentum gain. It results from the particle orbit crossing by a shock with the compression ratio r. Under the "favorable" magnetic configuration we understand the one where the Parker spiral field is roughly aligned with the field between the bow-shock and TS. Specifically, we assume that the B-field is out of plane on both sides of the TS surface, Fig. 6. For simplicity, the curved bow shock and TS are shown as planar shocks. Upstream of it, the particle inscribes an arc in the local fluid frame. The orbit's continuation downstream is more complex, as the motion electric field is not constant there and cannot be eliminated by the frame transformation. Indeed, the flow on the downstream side of the TS is established by its collision with the ISM flow downstream of the bow-shock. The resulting flow is deflected along the TS-bow-shock direction away from the flow stagnation region. In and around this region the flow speed is much lower than $U_{\rm SW}$ and we may neglect the effect of the outflow, that is the effect of the motion electric field on the 10-TV particles. In this case, the particle orbit is also a part of a circle in the frame fixed by the positions of the TS and bow shock, and, thereby the magnetic trap.

Assuming that a particle in the magnetic trap enters the wind cavity through the TS at an angle $\hat\alpha$ and returns at angle $\check\alpha$, as shown in Fig. 6, we shall obtain the momentum gain in terms of the entry phase upstream, ϕ :

$$\phi = -\tan^{-1}\left(\frac{\cos\hat\alpha\sqrt{1-U_{\rm SW}^2/c^2}}{\sin\hat\alpha + U_{\rm SW}/\hat v_\perp}\right), \qquad \text{(A1)}$$

and the upstream rotation phase, 2τ, where τ is a root of the following transcendental equation:

$$\cos(\phi+\tau)\,\frac{\sin\tau}{\tau} = \frac{U_{\rm SW}}{v_\perp}. \qquad \text{(A2)}$$

Here $v_\perp$ is the perpendicular to the B-field component of particle velocity and $U_{\rm SW} \ll c$. The equation above can be derived by assuming that while the particle makes an arc 2τ upstream of the TS the shock itself progresses to a distance $2\tau U_{\rm SW}/\omega_c$ in the upstream frame. Note that as long as particles are in the magnetic trap, their average pitch angle remains close to $\pi/2$ and we can set $v_\perp \approx c$. We represent the momentum gain as a ratio of the particle Lorentz factors after and before it visited the wind cavity

$$\eta = \frac{\check\gamma}{\hat\gamma} = \frac{1-(U_{\rm SW}/c)\cos(\phi+2\tau)}{1-(U_{\rm SW}/c)\cos\phi}.$$

After reentering the downstream space at the angle $\check\alpha$

$$\check\alpha = \cos^{-1}\left\{\frac{\sin[\phi+2\tau]\sqrt{1-U_{\rm SW}^2/c^2}}{1-(U_{\rm SW}/c)\cos[\phi+2\tau]}\right\}, \qquad \text{(A3)}$$

the particle gyrates around its guiding center fixed in the TS frame, as we assumed above. Eqs. (A1), (A2), and (A3) determine an iterated map $\hat\alpha \mapsto \hat\alpha'$ (Fig. 7). In the next cycle, the TS entrance angle $\hat\alpha' = \check\alpha$ will be different from $\hat\alpha$, in general, but after several such visits the exit angle $\check\alpha$ approaches the entrance angle $\hat\alpha$. In other words, the iterations converge to a fixed point $\check\alpha = \hat\alpha = \beta$. This fixed point is stable, since $|d\hat\alpha'/d\hat\alpha| < 1$ at $\hat\alpha = \beta$.

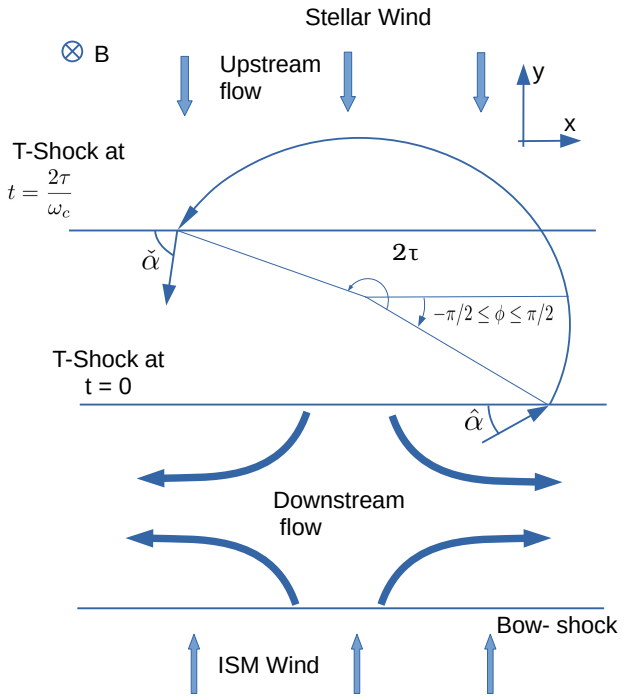


Figure 6. Mechanism of acceleration of particles entering the wind cavity from the downstream of the TS. Particles enter the upstream side of the TS from the astrosheath, propagate along an arc in the stellar wind frame, and return to the astrosheath. Positions of the TS (T-Shock) at these moments are shown with horizontal lines.

A.4. *Results and Application to Epsilon Eridani Star*

Since the stellar wind is nonrelativistic, $U_{\rm SW} \ll c$, from Eqs. (A1) and (A2) we find $\tau \approx \pi\left(1-U_{\rm SW}^2\right)/2 \approx \pi/2$ and

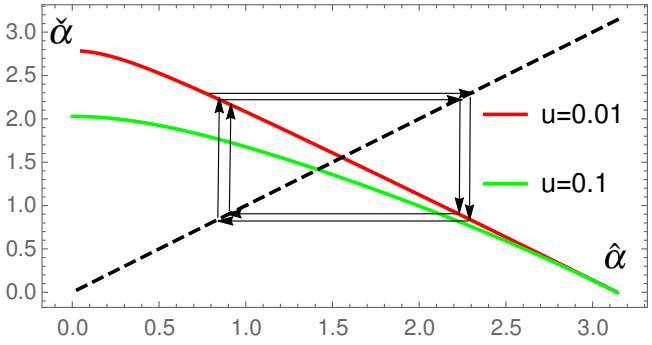


Figure 7. Iterated map $\hat{\alpha} \mapsto \hat{\alpha}'$. It is constructed by a superposition of the map $\hat{\alpha} \mapsto \check{\alpha}$ (shown with solid lines for two different stellar wind speed, $u = U_{\rm SW}/c$) and the identity map (shown with a dashed line, see text). Arrows show the first two iterations of an infinite series that ultimately converges to a fixed point. The case of a faster shock with $u = 0.1$ is also shown for comparison with a green line.

$\phi \approx \pi U_{\rm SW}/2$. Under these conditions, the energy gain tends to $\eta \approx 1 + 2U_{\rm SW}/c$. It corresponds to the energy gain of a particle specularly reflected from the medium moving at the speed $U_{\rm SW}$, as expected. The question that arises is for how long a particle can remain in the magnetic trap and keep gaining momentum $\Delta p_\perp/p_\perp = 2U_{\rm SW}/c$ after each rotation.

To give a simple answer to this question, we consider the energy range wherein the above acceleration mechanism operates. The upper bound is set by the particle gyroradius not to exceed the size of magnetic trap. Using the results of Wood et al. (2002), we may assume that the size of the trap across the field is $\sim 10^3$AU. As the field outside of the magnetic cavity should be enhanced according to the above considerations and the Axford-Crandfield effect (Axford 1972) to about 10 μG, particles of several tenths of TV can be confined to the cavity and accelerated, even though the field should be diminished inside.

Using the available data about the Epsilon Eridani star, we may also estimate the stellar wind velocity $U_{\rm SW}$ that determines the particle acceleration rate. The required parameters are the mass loss rate $\dot{M}$ which is about $30\dot{M}_\odot$ and the stand-off distance of TS being $R_{\rm SW} \sim 10^3$AU at its minimum on the upwind side of the moving star (Wood et al. 2002). Since these are very crude estimates, we simply assume that the Epsilon Eridani is moving through the ISM, similar to that around our heliosphere, that is with the same pressure and the ISM wind having nearly the same speed. Therefore, the ram pressure at the TS is also nearly the same: $\rho_{\rm SW}U_{\rm SW}^2 = \rho_\odot U_\odot^2$. From the mass ratio 30, we obtain $\rho_{\rm SW}U_{\rm SW}R_{\rm SW}^2 = 30\rho_\odot U_\odot R_\odot^2$, where the index SW refers to the Epsilon Eridani. We, therefore, obtain $U_{\rm SW}/U_\odot \simeq R_{\rm SW}^2/30R_\odot^2 \simeq 3$ and find that the momentum gain per cycle is $\Delta p_\perp/p_\perp = 2U_{\rm SW}/c \sim 10^{-2}$. We thus conclude that particles trapped in the magnetic cavity for a hundred of gyro-periods gain an additional energy comparable with that they gained by crossing the stellar bow shock.

REFERENCES

Abeysekara, A., Alfaro, R., Alvarez, C., et al. 2019, The Astrophysical Journal, 871, 96

Achterberg, A., Blandford, R. D., & Reynolds, S. P. 1994, A&A, 281, 220

Ackermann, M., Ajello, M., Albert, A., et al. 2014, PhRvL, 112, 151103, doi: 10.1103/PhysRevLett.112.151103

Adriani, O., Barbarino, G. C., Bazilevskaya, G. A., et al. 2011, *Science*, 332, 69, doi: 10.1126/science.1199172

Adriani, O., Akaike, Y., Asano, K., et al. 2019, PhRvL, 122, 181102, doi: 10.1103/PhysRevLett.122.181102

—. 2020, PhRvL, 125, 251102, doi: 10.1103/PhysRevLett.125.251102

Aguilar, M., Aisa, D., Alpat, B., et al. 2015a, PhRvL, 114, 171103, doi: 10.1103/PhysRevLett.114.171103

—. 2015b, PhRvL, 115, 211101, doi: 10.1103/PhysRevLett.115.211101

Aguilar, M., Ali Cavasonza, L., Alpat, B., et al. 2017, PhRvL, 119, 251101, doi: 10.1103/PhysRevLett.119.251101

Aguilar, M., Ali Cavasonza, L., Ambrosi, G., et al. 2018a, PhRvL, 120, 021101, doi: 10.1103/PhysRevLett.120.021101

Aguilar, M., Ali Cavasonza, L., Alpat, B., et al. 2018b, PhRvL, 121, 051103, doi: 10.1103/PhysRevLett.121.051103

Aguilar, M., Ali Cavasonza, L., Ambrosi, G., et al. 2020, PhRvL, 124, 211102, doi: 10.1103/PhysRevLett.124.211102

Aguilar, M., Ali Cavasonza, L., Ambrosi, G., et al. 2021, PhR, 894, 1, doi: 10.1016/j.physrep.2020.09.003

Ahn, H. S., Seo, E. S., Adams, J. H., et al. 2006, Advances in Space Research, 37, 1950, doi: 10.1016/j.asr.2005.09.031

Ahn, H. S., Allison, P. S., Bagliesi, M. G., et al. 2008, Astropart. Phys. , 30, 133, doi: 10.1016/j.astropartphys.2008.07.010

Ahn, H. S., Allison, P., Bagliesi, M. G., et al. 2009, ApJ, 707, 593, doi: 10.1088/0004-637X/707/1/593

—. 2010, ApJL, 714, L89, doi: 10.1088/2041-8205/714/1/L89

Alemanno, F., An, Q., Azzarello, P., et al. 2021, PhRvL, 126, 201102, doi: 10.1103/PhysRevLett.126.201102

Aloisio, R., Blasi, P., & Serpico, P. D. 2015, A&A, 583, A95, doi: 10.1051/0004-6361/201526877

An, Q., Asfandiyarov, R., Azzarello, P., et al. 2019, Science Advances , 5, doi: 10.1126/sciadv.aax3793

Atkin, E., Bulatov, V., Dorokhov, V., et al. 2018, *JETP Lett.* , 108, 5, doi: 10.1134/S0021364018130015

Atkin, E. V., Bulatov, V. L., Vasiliev, O. A., et al. 2019, *Astron. Reports*, 63, 66, doi: 10.1134/S1063772919010013

Axford, W. I. 1972, The Interaction of the Solar Wind With the Interstellar Medium. NASA Special Publication, ed. C. P. Sonett, P. J. Coleman, & J. M. Wilcox, Vol. 308, 609

Blandford, R. D., & Ostriker, J. P. 1978, ApJL, 221, L29, doi: 10.1086/182658

Blasi, P., Amato, E., & Serpico, P. D. 2012, PhRvL, 109, 061101, doi: 10.1103/PhysRevLett.109.061101

Boschini, M. J., Della Torre, S., Gervasi, M., et al. 2020a, ApJ, 889, 167, doi: 10.3847/1538-4357/ab64f1

—. 2020b, ApJS, 250, 27, doi: 10.3847/1538-4365/aba901

Brunetti, G., & Lazarian, A. 2007, MNRAS, 378, 245, doi: 10.1111/j.1365-2966.2007.11771.x

Burlaga, L. F., Ness, N. F., Berdichevsky, D. B., et al. 2019, Nature Astronomy, 3, 1007, doi: 10.1038/s41550-019-0920-y

Bykov, A. M. 2001, SSRv, 99, 317

Drury, L. O. 1983, Reports on Progress in Physics, 46, 973

Drury, L. O. C., & Strong, A. W. 2017, A&A, 597, A117, doi: 10.1051/0004-6361/201629526

Fang, K., Bi, X.-J., & Yin, P.-F. 2020, ApJ, 903, 69, doi: 10.3847/1538-4357/abb8d7

Fornieri, O., Gaggero, D., Guberman, D., et al. 2021, PhRvD, 104, 103013, doi: 10.1103/PhysRevD.104.103013

Grebenyuk, V., Karmanov, D., Kovalev, I., et al. 2019a, *Adv. Spa. Res.* , 64, 2546, doi: 10.1016/j.asr.2019.10.004

—. 2019b, *Adv. Spa. Res.* , 64, 2559, doi: 10.1016/j.asr.2019.06.030

Gry, C., & Jenkins, E. B. 2014a, A&A, 567, A58, doi: 10.1051/0004-6361/201323342

—. 2014b, A&A, 567, A58, doi: 10.1051/0004-6361/201323342

Gurevich, A. V. 1968, Soviet Journal of Experimental and Theoretical Physics, 26, 575

Hanusch, A., Liseykina, T. V., & Malkov, M. 2019, ApJ, 872, 108, doi: 10.3847/1538-4357/aafdae

Iroshnikov, P. S. 1964, Soviet Ast., 7, 566

Karmanov, D., Kovalev, I., Kudryashov, I., et al. 2020a, *Phys. Lett. B* , 811, 135851, doi: 10.1016/j.physletb.2020.135851

Karmanov, D. E., Kovalev, I. M., Kudryashov, I. A., et al. 2020b, *JETP Lett.* , 111, 363, doi: 10.1134/S002136402007005X

Kolmogorov, A. 1941, Akademiia Nauk SSSR Doklady, 30, 301

Kraichnan, R. H. 1965, Physics of Fluids, 8, 1385, doi: 10.1063/1.1761412

Lemoine, M. 2021, PhRvD, 104, 063020, doi: 10.1103/PhysRevD.104.063020

Malkov, M. 2018, Nuclear and Particle Physics Proceedings, 297-299, 20, doi: https://urldefense.proofpoint.com/v2/url?u=https-3A__doi.org_10.1016_j.nuclphysbps.2018.07.004&d=DwIGAw&c=-35OiAkTchMrZOngvJPOeA&r=cAjn_HZnw7abn1I20CJlybLNhQIAAa1c0pJptuYw2_c&m=iHcDBHTloCODAk4CjNFG-KoIt8Y-NMRwtukZt3e4NUj9j7M63_Wy77q8btnQ1xpB&s=KW1QHZzASOiURV3SYkAbiqu97EXZVJAGETrsijXp9oU&e=

Malkov, M. A. 1998, PhRvE, 58, 4911, doi: 10.1103/PhysRevE.58.4911

Malkov, M. A. 2017, Physical Review D, 95, 023007

Malkov, M. A., Diamond, P. H., & Sagdeev, R. Z. 2012, PhRvL, 108, 081104, doi: 10.1103/PhysRevLett.108.081104

Malkov, M. A., & Moskalenko, I. V. 2021, ApJ, 911, 151, doi: 10.3847/1538-4357/abe855

Malkov, M. A., & Sotnikov, V. I. 2022, arXiv e-prints, arXiv:2201.04199. https://arxiv.org/abs/2201.04199

Panov, A. D., Sokolskaya, N. V., Adams, J. H., J., et al. 2008, in Proc. 30th Int. Cosmic Ray Conf. (Merida), Vol. 2, 3–6. https://arxiv.org/abs/0707.4415

Panov, A. D., Adams, J. H., Ahn, H. S., et al. 2009, *Bull. Russian Acad. Sci., Physics*, 73, 564, doi: 10.3103/S1062873809050098

Porter, T. A., Jóhannesson, G., & Moskalenko, I. V. 2019, ApJ, 887, 250, doi: 10.3847/1538-4357/ab5961

Ptuskin, V. S., Moskalenko, I. V., Jones, F. C., Strong, A. W., & Zirakashvili, V. N. 2006, ApJ, 642, 902, doi: 10.1086/501117

Rangelov, B., Montmerle, T., Federman, S. R., Boissé, P., & Gabici, S. 2019, The Astrophysical Journal, 885, 105, doi: 10.3847/1538-4357/ab43e5

Seo, E. S., & Ptuskin, V. S. 1994, ApJ, 431, 705, doi: 10.1086/174520

Shu, F. H., Milione, V., Gebel, W., et al. 1972, ApJ, 173, 557, doi: 10.1086/151444

Sibeck, D. G., Lee, S. H., Omidi, N., & Angelopoulos, V. 2021, Journal of Geophysical Research (Space Physics), 126, e29201, doi: 10.1029/2021JA029201

Vladimirov, A. E., Jóhannesson, G., Moskalenko, I. V., & Porter, T. A. 2012, ApJ, 752, 68, doi: 10.1088/0004-637X/752/1/68

Webb, G. M., Axford, W. I., & Forman, M. A. 1985, ApJ, 298, 684, doi: 10.1086/163652

Wood, B. E., Müller, H.-R., Zank, G. P., & Linsky, J. L. 2002, The Astrophysical Journal, 574, 412

Yoon, Y. S., Ahn, H. S., Allison, P. S., et al. 2011, ApJ, 728, 122, doi: 10.1088/0004-637X/728/2/122

Yoon, Y. S., Anderson, T., Barrau, A., et al. 2017, ApJ, 839, 5, doi: 10.3847/1538-4357/aa68e4

Yuan, Q., Qiao, B.-Q., Guo, Y.-Q., Fan, Y.-Z., & Bi, X.-J. 2020, Frontiers of Physics, 16, 24501, doi: 10.1007/s11467-020-0990-4